

Two Dimensional Configuration and Temporal Evolution of Sparking discharges in Pulsars

RAHUL BASU ,¹ GEORGE I. MELIKIDZE ,^{1,2} AND DIPANJAN MITRA ,^{3,1}

¹Janusz Gil Institute of Astronomy, University of Zielona Góra, ul. Szafrana 2, 65-516 Zielona Góra, Poland.

²Evgeni Kharadze Georgian National Astrophysical Observatory, 0301 Abastumani, Georgia.

³National Centre for Radio Astrophysics, Tata Institute of Fundamental Research, Pune 411007, India.

Submitted to The Astrophysical Journal

ABSTRACT

We have investigated the evolution of a system of sparking discharges in the inner acceleration region (IAR) above the pulsar polar cap. The surface of the polar cap is heated to temperatures around 10^6 K and forms a partially screened gap (PSG) due to thermionic emission of positively charged ions from the stellar surface. The sparks lag behind the co-rotation speed during their lifetimes due to variable $\mathbf{E} \times \mathbf{B}$ drift. In a PSG the sparking discharges arise in locations where the surface temperatures go below the critical level (T_i) for ions to freely flow from the surface. The sparking commences due to the large potential drop developing along the magnetic field lines in these lower temperature regions and subsequently the back streaming particles heat the surface to T_i . The temperature regulation requires the polar cap to be tightly filled with sparks and a continuous presence of sparks is required around its boundary since no heating is possible from the closed field line region. We have estimated the time evolution of the sparking system in the IAR which shows a gradual shift in the spark formation along two distinct directions resembling clockwise and anti-clockwise motion in two halves of the polar cap. Due to the differential shift of the sparking pattern in the two halves, a central spark develops representing the core emission. The temporal evolution of the sparking process was simulated for different orientations of the non-dipolar polar cap and reproduced the diverse observational features associated with subpulse drifting.

Keywords: pulsars:

1. INTRODUCTION

The pulsar magnetosphere is characterised by a steady outflow of relativistic plasma along the open magnetic field lines. The majority of the electromagnetic radiation from pulsars arises within this outflowing plasma, including the radio emission that results from non-linear plasma instabilities (Melikidze et al. 2000; Gil et al. 2004; Lakoba et al. 2018; Rahaman et al. 2020). The outflowing plasma is also the source of the dense pulsar wind responsible for the pulsar wind nebulae (de Jager 2007; Kargaltsev et al. 2015). Detailed estimates have constrained the the radio emission to originate from heights of less than 10 percent of the light cylinder radius (von Hoensbroech & Xilouris 1997; Kijak & Gil 1998; Mitra & Rankin 2002; Mitra & Li 2004; Weltevrede & Johnston 2008; Krzeszowski et al. 2009; Mitra 2017). Thus the location of the plasma generation region is well inside the inner magnetosphere. The prototype for the plasma generation region is the inner vacuum gap (IVG) above the polar caps, extending to heights of ~ 10 -100 meters from the stellar surface, and potential difference of 10^{12} V across it (Sturrock 1971; Ruderman & Sutherland 1975). The outflowing plasma is generated as a series of sparking discharges due to creation of e^-e^+ pairs in presence of high magnetic fields and are accelerated to relativistic speeds in opposite directions by the large potential drop, setting up a cascading effect. The charges within each spark screen the electric potential till they leave the gap due to inertial motion, when the subsequent sparks are formed resulting in a non-stationary plasma flow.

There are certain limitations in the vacuum gap model of the inner acceleration region (IAR) above the polar cap. The back-flowing relativistic charges in the sparks heat up the surface to temperatures $\sim 10^6$ K which is close to

the critical level (T_i) for ionic¹ free flow from the surface (Cheng & Ruderman 1980; Jones 1986). As a result the IAR is not a complete vacuum but forms a partially screened gap (PSG) with a steady density of positively charged ions. It was shown by Gil et al. (2003) that in a PSG, where the ionic density (ρ_i) are as high as 90 percent of the Goldreich-Julian co-rotational density (ρ_{GJ} , Goldreich & Julian 1969), sparking discharges can develop in the IAR. The spark formation is governed by the surface temperature (T_S) with thermostatic self-regulation of the potential drop in the IAR. In a purely vacuum gap there is presence of unscreened potentials between sparks and hence the discharges cannot be confined at any location on the surface, but is expected to scatter in the direction opposite to the principal normal of the curvature of the local magnetic field lines (Cheng & Ruderman 1980). The thermostatic self-regulation in a PSG ensures that the sparking is limited to finite size with a typical length scale.

Other constraints on the physical properties of the IAR has been obtained from several detailed studies. The surface magnetic field above the polar cap is expected to be highly non-dipolar in nature. The efficiency of the pair cascade leading to the sparking discharge as well as the high multiplicity (10^5) of the outflowing plasma requires magnetic field lines with radius of curvature $\sim 10^5 - 10^6$ cm (Timokhin & Harding 2019), in contrast to $\sim 10^8$ cm for purely dipolar fields. The non-dipolar nature of the polar cap has also been supported by measurements of the thermal X-ray emission from the hot polar cap surface as well as simultaneous radio/X-ray studies of pulsars (Gil et al. 2008; Hermsen et al. 2013; Szary et al. 2017; Geppert 2017; Hermsen et al. 2018; Arumugasamy & Mitra 2019; Sznajder & Geppert 2020; Pétri & Mitra 2020). The sparks are expected to undergo variable $\mathbf{E} \times \mathbf{B}$ drift in the IVG which results in the well known observational behaviour of subpulse drifting (Weltevrede et al. 2006; Basu et al. 2016) in the pulsed radio emission. It has been suggested that the sparks in the IAR rotate around the magnetic axis (Ruderman & Sutherland 1975; Szary & van Leeuwen 2017), however, in our previous work (Basu et al. 2020b, hereafter Paper I) it was shown that in the absence of any external electric field, the sparks in IAR would lag behind co-rotation speed during their lifetimes. The phase behaviour associated with drifting periodicity reflects the dynamics of the sparking process in the IAR (Basu & Mitra 2018; Basu et al. 2019a). In Paper I the lagging behind motion of the sparks along with the non-dipolar nature of the surface fields was used to simulate different categories of phase behaviour associated with drifting (Basu et al. 2019a).

One important observational feature of the drifting behaviour is the absence of drifting in the central core region of the profile window (Rankin 1986; Basu et al. 2019a), and cannot be explained by lagging behind motion of the sparks throughout the polar cap. It was recognized in Paper I that the lagging behind scenario is restricted by the presence of polar cap boundaries beyond which no spark can be formed in the closed field line region. The thermal regulation of the hot polar cap surface requires a continual presence of sparking discharges along the boundary since no additional heating is possible from the closed field lines on the other side. In this work we have expanded on the ideas presented in Paper I by including the effects of the polar cap boundary on the sparking configuration. A two-dimensional model of the sparking discharges in a PSG is presented and we explore its evolution with time. The constraints from the polar cap boundary coupled with the lagging behind co-rotation motion of the sparks during their lifetimes introduce two distinct trajectories for the temporal evolution of the sparking distribution. One half exhibits a clockwise evolution while the other half shows an anti-clockwise behaviour. The differential shift of the sparking pattern in the two halves as well as the tightly packed nature of sparking distribution implies that heating location at the center is stationary in most configurations of non-dipolar polar caps and accounts for the absence of drifting in the core component.

In the following sections we present the details of the model and simulations of tightly packed sparking distribution in the IAR starting with the physical characteristics of sparks in section 2. Section 3 demonstrates the effect of the polar cap boundary on the location of the subsequent sparks and their shifts to be in opposite directions in two halves of the polar cap. The two-dimensional configuration of the sparking discharges and their temporal evolution is explored in section 4. We have used the estimated sparking distribution and its time evolution to simulate the subpulse drifting behaviour. The drifting behaviour for different orientations of the surface non-dipolar magnetic fields is shown in section 5. A short discussion summarising the implications of this work is presented in section 6.

2. PHYSICAL PARAMETERS OF SPARKS IN A PARTIALLY SCREENED GAP

The details of the spark formation in a PSG was first presented in Gil et al. (2003) and have been further explored in several subsequent works (Gil et al. 2006; Szary 2013; Szary et al. 2015; Mitra et al. 2020, Paper I). In this section we summarize the different physical parameters like the spark size, the time scales associated with the sparking process,

¹ We are considering stars where $\Omega \cdot \mathbf{B} < 0$ and have positive charge densities above the polar caps such that a IAR gap can be established.

etc., that has been estimated in these earlier works and will be used later to understand the sparking configuration in the IAR.

2.1. Size of spark

The charge density above the polar cap is limited by the co-rotational density, $\rho_{GJ} = \Omega B / 2\pi c$, which is many orders of magnitude lower than the density of ions on the stellar crust. As a result a sufficiently heated polar cap can sustain a free flow of ions from the tail end of the surface charge distribution at the critical Temperature, $T_i \approx \epsilon_i / 30k$, here ϵ_i is the binding energy of ions and k is the Boltzmann constant (Cheng & Ruderman 1980). For surface temperatures, $T_S < T_i$, a charge depleted acceleration region is formed which is populated by ions with density $\rho_i < \rho_{GJ}$. A sparking discharge is setup in this region which heats the surface till $T_S = T_i$ is reached and the ionic free flow is restored terminating the spark. The effective potential drop ΔV_{PSG} across each spark is given as :

$$\Delta V_{PSG} = \frac{4\pi\eta b B_d \cos \alpha_l}{Pc} h_{\perp}^2 \quad (1)$$

here $\eta = 1 - \rho_i / \rho_{GJ} = 1 - \exp[30(1 - T_i / T_S)]$, $b = B_s / B_d$ where B_s is the non-dipolar surface magnetic field and $B_d = 2 \times 10^{12} (P \dot{P}_{-15})^{0.5}$ G, the equivalent dipolar field, α_l is angle between the local magnetic field and the rotation axis, h_{\perp} is the perpendicular radius of the spark and P and \dot{P} are the pulsar rotation period and period derivative respectively. The total energy deposited per unit area on the surface of the polar cap by the back streaming electrons can be estimated by multiplying the energy of each electron with the particle flux in the spark $P_S = (e\Delta V_{PSG}) \times (\eta n_{GJ}c)$. Equating the deposited energy per unit area with the energy radiated from the heated surface, $P_S = \sigma T^4$, the typical radius of a spark can be estimated as

$$h_{\perp} = 260 \frac{T_6^2}{\eta b (\cos \alpha_l)^{0.5}} \left(\frac{P}{\dot{P}_{-15}} \right)^{0.5} \text{ cm}, \quad (2)$$

where the surface temperature $T_S = T_6 \times 10^6$ K.

2.2. Timescales associated with Sparking

There are two relevant time scales associated with the sparking process, the heating time (t_s) or spark duration, the time taken by the sparking process to heat the surface to the critical temperature, and the cooling time (t_c) which is the time elapsed between the cessation of the sparking process and the surface to cool sufficiently for the next spark to commence. These estimates require understanding the physical properties of the neutron star crust where the heating is taking place. At temperatures around million Kelvin the crust permeated by highly non-dipolar magnetic fields have been shown to exist in a crystalline state and the surface density (ρ_s) can be calculated in such cases as (Lai 2001) :

$$\rho_s \simeq 561 A Z^{-3/5} b^{6/5} \text{ g cm}^{-3}, \quad (3)$$

Where A is the mass number and Z the atomic number of the constituent atoms in the crust. The crust is made up of iron atoms with $A = 56$ and $Z = 26$ and the density is $\rho_s = 4.45 \times 10^3 b^{6/5} \text{ g cm}^{-3}$. The durations of heating and cooling of the crust depends on the depth of heat deposition and can be estimated using the radiation length $y = 14 \text{ g cm}^{-2}$ for iron ions. The corresponding depth is given as

$$L_R = y / \rho_s \simeq 3.15 \times 10^{-3} b^{-6/5} \text{ cm}. \quad (4)$$

The heat can be deposited up to a depth of several times L_R , $L \approx 10^{-3} \text{ cm}$ (Gil et al. 2003).

The total energy carried by the back-streaming particles is used to heat the crust with specific heat per unit volume C_H to a depth of L , $C_H L \partial T / \partial t \simeq C_H L T / t_s$, assuming uniform heating. The specific heat of the crust has contribution from the lattice vibrations as well as the free electrons and is given as :

$$C_H \approx 4.4 \times 10^{12} \rho_6 (1 + 0.024 \rho_6^{-2/3} T_6) \approx 2 \times 10^{10} b^{6/5} (1 + 0.89 b^{-4/5} T_6) \text{ erg K}^{-1} \text{ cm}^{-3}. \quad (5)$$

The sparking timescales can be estimated from the above expressions as :

$$t_s \approx 30 (1 + 0.89 b^{-4/5} T_6) T_6^{-3} \text{ } \mu\text{sec.} \quad (6)$$

The sparks lag behind co-rotation velocity and the total distance during the lifetime is $h_s = \eta v_{crt} t_s$. The co-rotation velocity was estimated in Paper I to be around 10^6 cm s^{-1} resulting in $h_s \approx 10 \text{ cm}$.

Finally, in order to estimate the cooling time scale the heat transport equation is used

$$C_H \frac{\partial T}{\partial t} = \frac{\partial}{\partial l} \left(\kappa \frac{\partial T}{\partial l} \right) \quad (7)$$

where κ is the thermal conductivity of the crust. The surface layer for heat penetration is very thin and can be considered to have a uniform heat conductivity. The partial differential equation can be approximated as $\partial T / \partial t \approx T / t_c$ and $\partial^2 T / \partial^2 l \approx T / L^2$. This gives an order of magnitude estimate of the cooling time scale as

$$t_c = \left(\frac{L^2 C_H}{\kappa} \right) \quad (8)$$

In the outermost layers of the neutron star the heat transport is primarily dominated by the electronic transfer and for $b \sim 10$ the estimated $\kappa \sim 10^{12} \text{ erg cm}^{-1} \text{ s}^{-1} \text{ K}^{-1}$ (Gil et al. 2003). Hence, the cooling timescale of the polar cap is around 100 nsec which is more than two orders of magnitude shorter than the duration of sparks. It is possible for the subsequent sparking process to commence near the previous spark soon after it dies as the surface cools almost instantaneously.

3. SPARK FORMATION AND EFFECT OF POLAR CAP BOUNDARY

3.1. *Sparking in IAR*

In the PSG model the polar cap is positively charged ($\mathbf{\Omega} \cdot \mathbf{B} < 0$) with the surface temperatures maintained around the critical level for free flow of ions (T_i) due to thermostatic regulation from sparking discharges. When the surface temperature ($T_S \sim 10^6 \text{ K}$) is above T_i there is a steady outflow of positively charged ions from the stellar surface with density ρ_{GJ} , screening the potential drop along the IAR. If the temperature becomes lower than T_i the ionic density drops below ρ_{GJ} and a large potential drop appears along the IAR. As a result sparking discharges with cascading $e^- - e^+$ pairs are setup, with the pairs separated by the large potential difference. The electrons are accelerated downwards and heat the surface while the positrons are accelerated away from the surface and give rise to the outflowing plasma. The sparks grow in size till sufficient pairs are produced and the surface is heated to $T_S \gtrsim T_i$, thereby screening the potential drop across the IAR and terminating the spark. The typical lifetime of a spark is around 30 μsec (Eq.6) during which the spark grows both vertically and laterally (h_\perp in Eq.2) forming a cylindrical plasma column. The point of maximum heating lies at the center of the spark and falls off gradually towards the edge with no sharp boundaries in the temperature distribution below the spark. It has been shown in Paper I that the sparking plasma column during their lifetimes lag behind the co-rotation motion of the pulsar. As a result the maximally heated point at the termination of the spark is shifted by a small distance h_s opposite to the co-rotation direction. The dense plasma column after the termination of sparking leaves the IAR in about $\sim 300 \text{ nsec}$ which is comparable to the cooling time of the surface (Eq.8) and is much shorter than the duration of the sparks. In the absence of any other constraints the subsequent spark forms immediately at the location of maximum heating (hence fastest cooling), shifted by a distance h_s , resulting in an apparent drift motion.

If the size of the polar cap is larger than the lateral size of a spark then thermal regulation of the surface requires the presence of a system of tightly packed sparks in the IAR. There are no hard borders expected between adjacent sparks and the region near their edges are heated by particles from all surrounding sparks. The polar cap has a well defined boundary separating the open and closed magnetic field line regions. The closed field line region has constant ρ_{GJ} charge density and hence it is not possible to have sparking in the closed field line region with the boundary cutting across a spark, i.e. no spark can be formed straddling the boundary between the open and closed field line regions. The continuous heating of the surface around the boundary region requires an annular band of tightly packed sparks to be formed closely bordering the boundary. In order to ensure the effective heating of the surface to continue, no gaps can appear in the normal direction away from the boundary to the nearest spark during the lagging behind evolution of the sparking process. As a result the lagging behind motion of the sparking pattern is constrained by the polar cap boundary and subsequent sparks can only evolve around the annular ring either in the clockwise or anticlockwise manner (see section 3.2). If there is space for more than one ring of sparks in the polar cap, the presence of the outer band constrains the inner sparks to also be arranged in a nested inner concentric ring touching the outer sparking

band in a closely packed setup. The effective heating of the surface requires the sparks in the inner ring to not have any gaps with the outer ring in the normal direction, thereby constraining the subsequent sparking pattern to evolve around the inner ring. Depending on the availability of space, multiple contiguous rings of increasingly smaller radius will be formed in this setup with sparks constrained to evolve around each ring, till there is space for only a single spark at the center. There is no space for evolution of sparking at the center and after the previous spark heats the surface above T_i and is extinguished, the next spark is formed around the same location after the surface cools down. The size of the central spark depends on the available space at the center and can be smaller than a typical spark. The arrangement of sparks in concentric rings around a central spark is consistent with the core-cone nature of the average radio emission beam (Rankin 1990, 1993; Gil et al. 1993), where the pulsar emission is arranged in concentric rings of conal emission around a central stationary core. The lifetimes of individual sparks are much shorter than the apparent drift motion of the sparking pattern which evolve over several seconds. Hence, the observed drifting behaviour reflects the change in the sparking pattern and is not associated with motion of individual sparks.

3.2. Effect of Polar Cap boundary on Sparking

Figure 1a shows a schematic of the evolution of the sparking process along the boundary. Initially the sparks (red outline) are formed close to each other in a tightly packed configuration around a point (red point) on the boundary which is maximally heated by particles from both sparks. During their lifetimes the sparks shift by an average distance h_s opposite to the co-rotation direction (dotted black outline). At the end of the life cycle the location of the maximally heated point (open black circle) shifts around the boundary due to the drift motion. After the surface cools down the next sparks are formed around this shifted point in the boundary resulting in an effective shift of the sparking pattern by a distance h_D along the boundary of the polar cap.

The angular shift (θ_{sft}) in the drift direction of the sparking pattern at different points on the boundary is related to the spatial shift (h_D) at a point specified by the polar angle (θ_{PC}) as :

$$\theta_{sft} = h_D / \sqrt{(a_{cap}^2 \sin^2 \theta_{PC} + b_{cap}^2 \cos^2 \theta_{PC})}, \quad (9)$$

here a_{cap} and b_{cap} are the major and minor axes of the elliptical polar cap with $a_{cap} = b_{cap} = R_{cap}$ for a circular case. The shifts in the sparking pattern along the entire polar cap boundary is shown in Figure 2 corresponding to, (a) circular polar cap with the sparks lagging behind co-rotation along the x-axis, (b) circular polar cap with the co-rotation direction making a 45° angle in the x-y plane, (c) elliptical polar cap with eccentricity 0.6 and major axis along the x-axis, and (d) elliptical polar cap with eccentricity 0.6 and major axis along the y-axis. The shift is maximum when the direction of co-rotation is tangential to the curvature of the boundary and goes to zero when co-rotation is normal to the boundary. In all cases there are two distinct regions of sparking evolution bounded by the points where the co-rotation direction is normal to the elliptical/circular boundary of the polar cap. In one half the shifts are in the negative direction which signify a clockwise shift of the sparking pattern, while in the other half the shifts are positive resembling an anti-clockwise shift. In the elliptical polar caps the maximum shifts are flatter or steeper compared to the circular case depending on the orientation of the major axis. In realistic situations the differential shifts will be averaged out due to finite size of the sparks, as the next spark can only form in the available space between two sparks and an average shift will be seen over time. We expect two distinct evolution pattern of the sparking discharges along the rim of the polar cap showing clockwise behaviour in one half and anti-clockwise evolution in the other half. We have used this insight about the evolution pattern to understand the two dimensional configuration of the sparking system.

4. THE SPARKING CONFIGURATION AND ITS TEMPORAL EVOLUTION

The distribution of sparks on the polar cap surface in the presence of a PSG have the following constraints:

1. A continuous presence of sparking is required bordering the boundary of the polar cap for effective thermal regulation.
2. The sparks are as tightly packed as possible within the IAR.
3. There are two distinct direction of sparking evolution with one half showing a clockwise shift in the pattern and the other half an anti-clockwise shift.

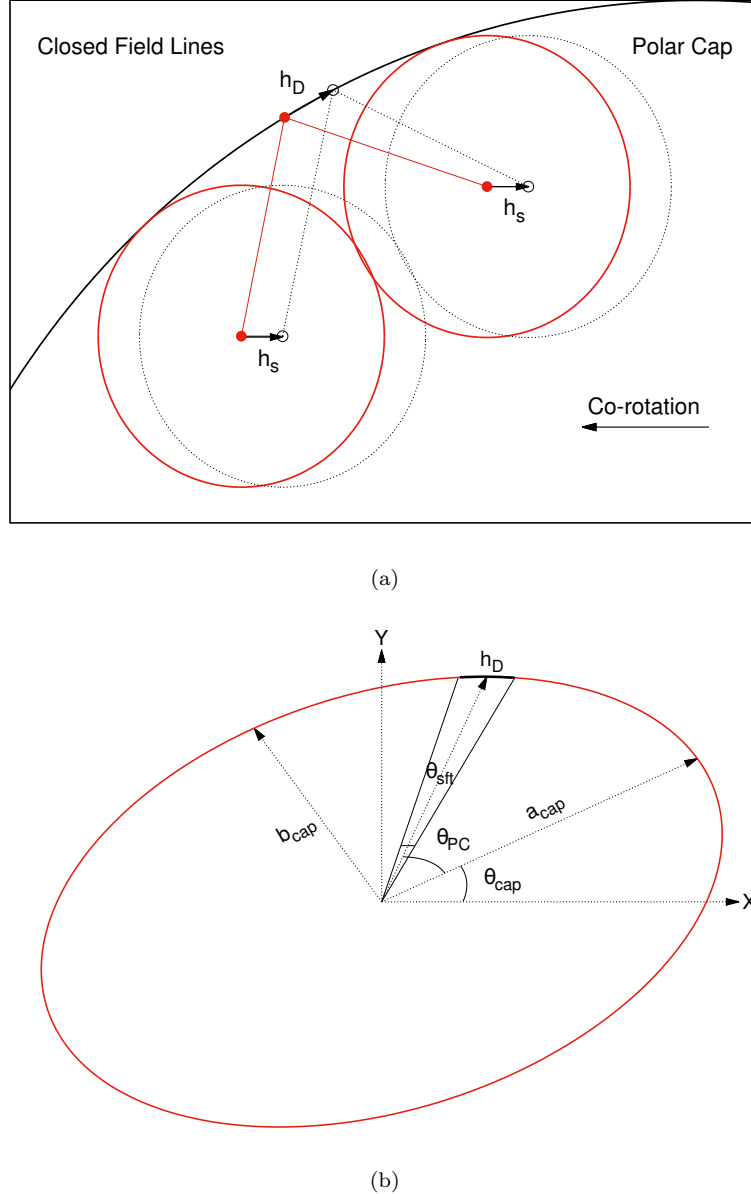


Figure 1. (a) The upper panel shows a schematic of the evolution of the sparking pattern along the polar cap boundary due to drifting of the sparks. The black curved line is the boundary of the polar cap where two sparks (red circles) develop around a maximally heated point (red dot) on the boundary. The sparks drifts by a distance h_s during their lifetimes as they lag behind the co-rotation direction. The maximally heated point (open black circle) at the end of the sparking process shifts by a distance h_D due to the drifting of the sparks. After the surface cools down the subsequent sparks are formed around the shifted point (open black circle) resulting in a shift of the sparking pattern. (b) The lower panel shows a schematic of the elliptical polar cap with major axis a_{cap} , minor axis b_{cap} and inclined at an angle θ_{cap} in the x-y plane. The spatial shift h_D along the boundary of the polar cap at a point specified by the polar angle θ_{PC} corresponds to the angular shift θ_{sft} .

The first condition requires the presence of an annulus of sparks bordering the boundary of the polar cap in a tightly packed configuration. The second condition ensures that in the interior of the polar cap the sparks are also formed in concentric layers with a single spark at the center. The central spark may differ in size depending on the available space. Finally, the third condition associated with subpulse drifting requires the sparking pattern in each concentric layer to shift in two different directions in two halves resembling a clockwise and anti-clockwise shift. The bounding points of the two layers are locations where the lagging behind co-rotation direction is normal to the concentric ring,

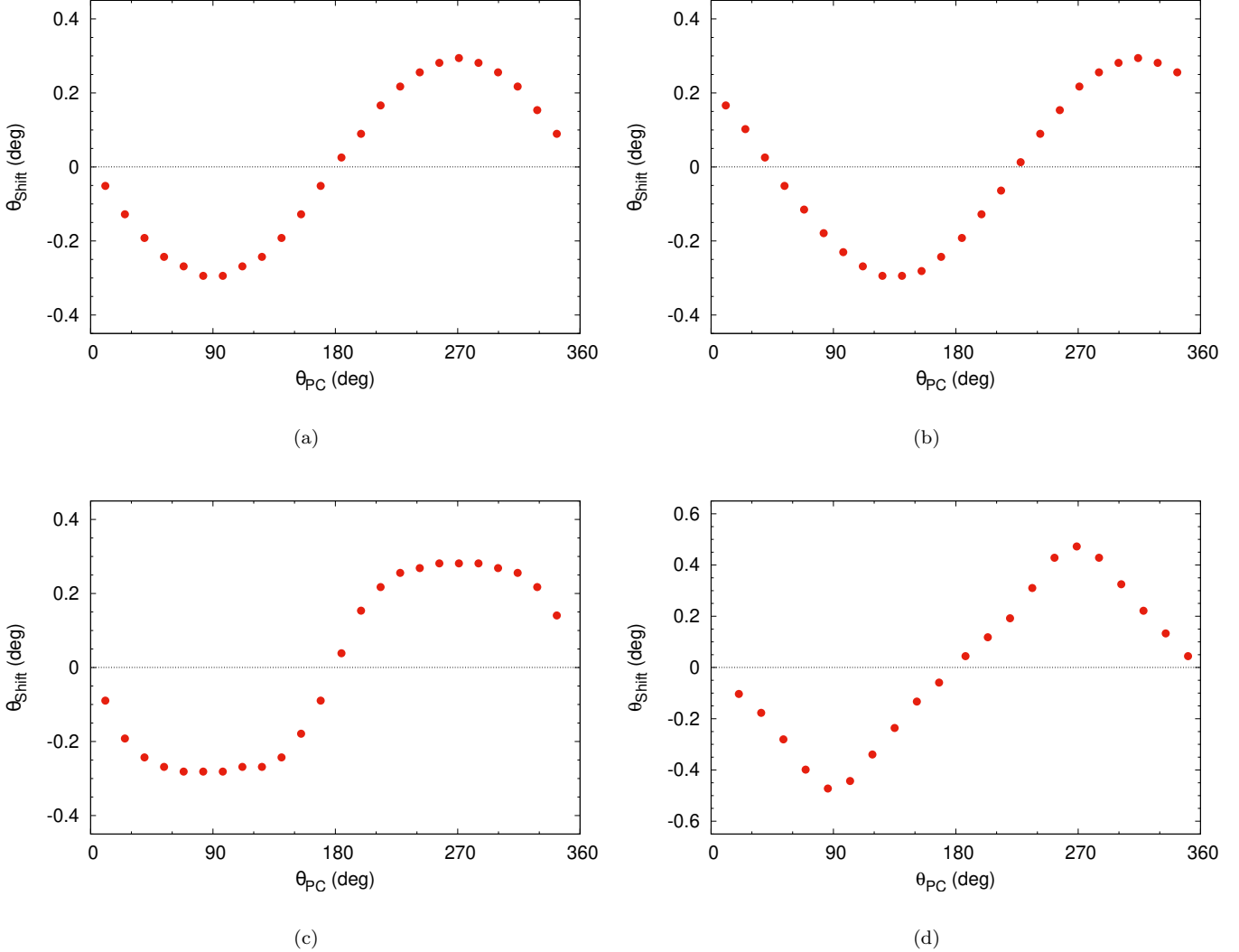


Figure 2. The figure shows the angular shift in the sparking pattern around the entire boundary of the polar cap (θ_{PC}). The panels in (a) and (b) represent circular polar caps where the sparks lag behind the co-rotation direction along the x-axis in case (a), while the sparks lag behind co-rotation along an axis which makes a 45° angle in the x-y plane in case of (b). In panels (c) and (d) examples of elliptical polar caps are shown with eccentricity 0.6 and sparks lagging behind along the x-axis in both cases. In panel (c) the major axis is oriented along the x-axis while in panel (d) the major axis is oriented along the y-axis.

the starting point being the inward normal and the ending point the outward normal. As the sparking pattern shifts away/towards the bounding points smaller empty spaces may open up in these regions. A spark appears in these locations due to the temperature going below the critical level, and as a consequence the potential drop appears, to start the sparking process. But there is heating in the surrounding regions from the sparks on either side of this location and hence the potential drop across it is lower, resulting in smaller sparks. Due to differential motion around it the central spark is not expected to show any shift but reappear around the same location depending on the surface heating requirements.

In a purely dipolar magnetic field configuration the polar cap boundary can be approximated to be circular in shape. However, as discussed in the introduction a number of detailed observations have revealed the polar cap to be non-dipolar in nature. In this work the non-dipolar nature of the surface field is modelled by considering a combination of magnetic dipoles of different strengths (see section 5). A large star centered dipole is used to reproduce the largescale magnetic field away from the stellar surface, while a weaker dipole is placed close to the polar cap to match the surface field strength as well as the estimated polar cap size (Gil et al. 2002; Basu et al. 2020b). In this configuration the

boundary of the non-dipolar polar cap is elliptical in shape with the direction of elongation depending on the location of the surface dipole. Although the magnetic field configuration considered in this work provides a convenient setup for estimating the non-dipolar surface magnetic field, it is not an unique solution. But the sparking evolution presented here should be applicable to polar caps with well defined continuous boundaries. An elliptical polar cap is defined by a major axis (a_{cap}), a minor axis (b_{cap}) and angle of inclination of the major axis in the x-y plane (θ_{cap}). The potential drop across the sparks are expected to vary along the different axes in elliptical polar caps and we approximate the spark shape to resemble the polar cap with major axis a_{sprk} , minor axis $b_{sprk} = a_{sprk}b_{cap}/a_{cap}$ and inclination angle θ_{cap} , such that $\sqrt{a_{sprk}b_{sprk}} \approx h_{\perp}$. The sparks are unlikely to have sharp boundaries but are expected to have a peak density and spread out till the surface is heated by an adjacent spark. The number of tracks of the concentric sparking trajectories in addition to the central core is $N_{trk} = \text{Int}(a_{cap}/a_{sprk})$. The maximum number of sparks that can be accommodated within any concentric annulus within the polar cap is given as :

$$\begin{aligned} N_{sprk}^i &= \text{Int} (F(a_{out}^i b_{out}^i - a_{in}^i b_{in}^i) / (a_{sprk} b_{sprk})) . \\ a_{out}^i &= a_{cap} - 2(i-1)a_{sprk}, \quad a_{in}^i = a_{out}^i - 2a_{sprk}, \\ b_{out}^i &= b_{cap} - 2(i-1)b_{sprk}, \quad b_{in}^i = b_{out}^i - 2b_{sprk}. \end{aligned} \quad (10)$$

Here $i = 1, 2, \dots, N_{trk}$ and F is a scaling factor for maximum packing which we find to be around 0.75. A series of sparks are setup along each of these concentric regions whose angular size is $\theta_{sprk}^i = 2\pi/N_{sprk}^i$, and their centers lie on the ellipse specified by $a_{trk}^i = (a_{out}^i + a_{in}^i)/2$ and $b_{trk}^i = (b_{out}^i + b_{in}^i)/2$. As specified before the dynamics of the evolution of the sparking pattern follows two different directions in two halves. In one half the next sparks are formed shifted by an angle $\theta_u^i = -h_D/\sqrt{a_{trk}^i b_{trk}^i}$ and in the other half by the angle $\theta_d^i = +h_D/\sqrt{a_{trk}^i b_{trk}^i}$, here h_D being the average shift of the sparking pattern which is constant for all i . Finally, smaller sparks are set up at either ends whose size is variable depending on the available space between the two trajectories.

The two dimensional sparking configuration for a circular polar cap, where $a_{cap} = b_{cap}$, with lagging behind co-rotation direction along the x-axis is shown in Figure 3. The sparking pattern evolves to resemble a clockwise shift in the upper half and an anti-clockwise shift at the lower half. The two regions are separated at the points where the co-rotation direction is normal to the circle, i.e, at $\theta_{PC} = 0^\circ, 180^\circ$ where θ_{PC} is represents the polar angle. As the spark pattern from either side shift away from $\theta_{PC} = 180^\circ$, a gap opens up which in certain cases is smaller than the size of a fully formed spark and smaller size sparks are formed. Similarly, at $\theta_{PC} = 0^\circ$, the available space reduces due to the encroachment from either side leading to smaller sparks. We have assumed that no phase difference exist between the shifts in the upper and lower halves. However, the sparks in these two regions evolve independently and can have any arbitrary phase difference between them.

5. MODELLING SUBPULSE DRIFTING

The evolution of the sparking distribution in the IAR is seen as the phenomenon of subpulse drifting in the pulsar radio emission. We have used the model of the two dimensional sparking distribution presented in the previous section to simulate the different drifting behaviour observed in pulsars. The process of generating a single pulse sequence from a pulsar with non-dipolar polar cap has been presented in Paper I and is summarized below.

The non-dipolar magnetic field in the polar cap is modelled using a large star centered dipole which dominate the magnetic field away from the star surface along with one or more surface dipoles which determine the magnetic field structure at the polar cap (Gil et al. 2002). We use a spherical co-ordinate system with the origin located at the center of the neutron star and the rotation axis along $\theta = 0^\circ$. The star centered dipole located at the origin is specified as $\mathbf{d} = (d, \theta_d, 0^\circ)$, where d represents the dipole moment and θ_d the inclination angle between the rotation and magnetic axis of the star. The surface dipoles are represented as $\mathbf{m}_i = (m^i, \theta_m^i, \phi_m^i)$, where $i = 1, 2, \dots, N$ in case more than one is used, with dipole moments $m^i = 0.001 - 0.05d$ much smaller than the star centered dipole, and the orientation of each dipole specified by the angles θ_m^i and ϕ_m^i . The surface dipoles are located at $\mathbf{r}_i = (r_s^i, \theta_s^i, \phi_s^i)$ close to the surface with $r_s^i = 0.95R_S$, $R_S = 10$ km is the neutron star radius, while the angles θ_s^i and ϕ_s^i can be varied to shift the location away from the purely dipolar polar cap. At a distance of $\sim 30R_S$ the contribution of surface dipole moments becomes negligible and the magnetic field is largely dipolar with contribution from \mathbf{d} . The opening angle corresponding to the last open dipolar field line at $30R_S$ is used to estimate the outline of the modelled polar cap surface by numerically solving the magnetic field line equations (see Paper I for details). The elliptical outline of the polar cap is estimated using non-linear Least Square fits (Press et al. 1992) to obtain a_{cap} , b_{cap} and θ_{cap} and the location of the center defined by θ_{cap}^c , ϕ_{cap}^c .

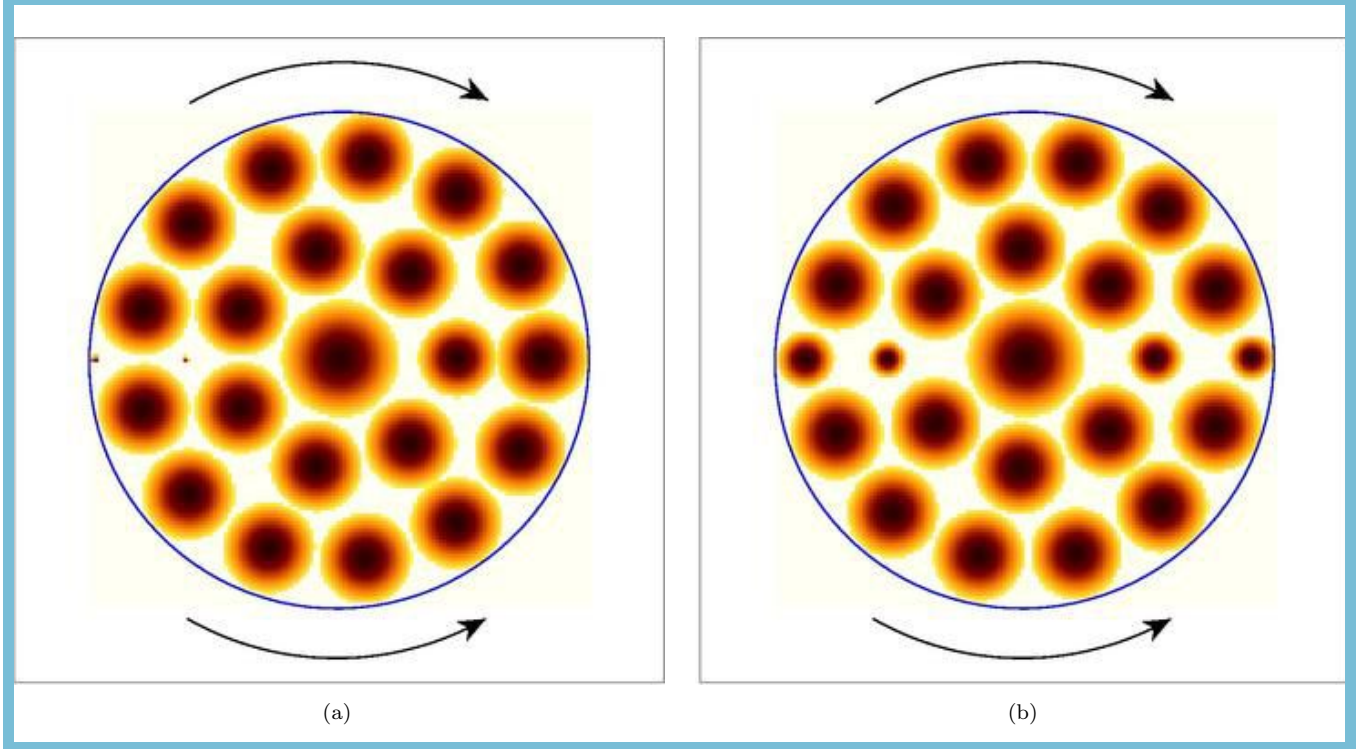


Figure 3. The figure shows two different snapshots of the distribution of sparking on a circular polar cap. The sparks are arranged within two concentric rings from the boundary and contains a central spark to form a tightly packed configuration. The sparking pattern evolves with time to show a clockwise shift in the upper half and a anti-clockwise shift in the lower half (see arrows) around the central spark. Smaller sparks are formed at the edges when the available space is less than the spark size but the surface still requires thermal regulation. The sparks in the figures do not have sharp borders, which are drawn primarily as guidelines to show the distinction between adjacent sparks.

An animation showing the evolution of the sparking configuration with time is available.

As the pulsar rotates the pulsed emission is seen when the line of sight (LOS) passes through the open field line across the radio emission region. The pulsar profile shape and the drifting behaviour is dependent on the LOS cut across this emission beam. The LOS is defined by the angle β which is the minimum angle between the axis of the star centered dipole and LOS. In the spherical co-ordinate system defined at the center of the neutron star, with the rotation axis aligned along the z-axis, the track of the LOS and consequently a train of pulsed emission is obtained by continuous change in the coordinate $\phi = 2\pi t/P$, for a fixed azimuth angle $\theta = \theta_d + \beta$. The non-dipolar polar cap is usually shifted from the dipolar case with the magnetic field lines twisting as they connect with the dipolar emission region around $10 - 100 R_S$. As a result the outline of the LOS gets modified as it traverses the sparking distribution resulting in different drifting behaviour for different surface magnetic field configurations. Once the LOS enters the open field line region the corresponding field line at the surface is estimated by numerically solving the magnetic field line equations. The sparking intensity at that point on the surface is estimated and recorded. It is assumed that the radio emission intensity follows that of the sparking, but in realistic cases the radio emission in the subpulses are a result of non-linear plasma processes (Melikidze et al. 2000) which introduces additional features. As the LOS traverses the extent of the pulse window an intensity pattern due to the sparking distribution is obtained and forms the single pulse. In subsequent rotations the sparking distribution evolves and gives different intensity patterns, reflecting the drifting behaviour.

In order to estimate the two dimensional sparking distribution a Cartesian $x'y'$ -plane² is defined to contain the elliptical polar cap with origin at the center of the ellipse. The boundary of the upper and lower halves of the polar cap signifying clockwise and anti-clockwise evolution of the sparking pattern is specified by the angles $\theta'_s = 3\pi/2 - \phi_{cap}^c$

² The primed co-ordinates are used to distinguish from the star centered co-ordinate system used for estimating the LOS traverse.

Table 1. The physical parameters of elliptical polar cap

	a'_{cap} (m)	b'_{cap} (m)	θ'_{cap} ($^{\circ}$)	θ^c_{cap} ($^{\circ}$)	ϕ^c_{cap} ($^{\circ}$)	b	$\cos \alpha_l$	η
Coherent	127.6	80.4	45.9	16.2	5.3	~ 4	~ 0.85	0.038
Phase-Stat	75.3	21.6	52.4	51.2	17.9	~ 19	~ 0.8	0.021
Bi-drift	62.2	36.1	148.5	3.2	100.1	~ 26	~ 0.79	0.013

and $\theta'_e = \pi/2 - \phi^c_{cap}$, here θ' is the polar angle in the $x'y'$ -plane. The sparking pattern diverges away from θ'_s and converges toward θ'_e . We have assumed a Gaussian distribution of intensity for each spark with elliptical symmetry :

$$I_{sprk}(x', y') = I_0 \exp \left(-\frac{1}{2} \left[(x' - x'_c)^2 / a_{sprk}^2 + (y' - y'_c)^2 / b_{sprk}^2 \right] \right) \quad (11)$$

Here I_0 is the peak intensity of spark and x'_c, y'_c corresponds to the center of the spark. The sparks do not have sharp borders and the intensity pattern is drawn primarily as guidelines to show the distinction between adjacent sparks. The location of the sparks within the elliptical polar cap and the evolution of their distribution with time is described in the previous section.

Similar to Paper I we have considered three different magnetic field configurations whose behaviour represent the three distinct observational classes of subpulse drifting, viz., coherent phase-modulated drifting, phase stationary drifting and Bi-drifting with opposite drift directions in different parts of the emission window (see Basu et al. 2019a). We present below the physical characteristics of the PSG for each magnetic field configuration, the temporal evolution of the two dimensional sparking configuration and the simulated single pulses showing subpulse drifting.

5.1. Coherent Phase-Modulated drifting

Coherent phase-modulated drifting is the prototype of the subpulse drifting behaviour with the subpulses showing a systematic shift throughout the entire pulse window. These are mostly associated with LOS traverses towards edge of the emission beam and seen in pulsar average profiles with single or double conal components (Rankin 1986; Basu et al. 2019a). In Paper I the magnetic field configuration used to demonstrate this behaviour consisted of a star centered dipole $\mathbf{d} = (d, 15^{\circ}, 0^{\circ})$ and one surface dipole $\mathbf{m} = (0.001d, 0^{\circ}, 0^{\circ})$ located at $\mathbf{r} = (0.95R_S, 18.86^{\circ}, 10.99^{\circ})$. The dipolar magnetic axis is tilted by an angle 15° with the rotation axis while the non-dipolar polar cap is located around 5° away in the ϕ -axis from the dipolar polar cap.

The polar cap is elliptical in shape with the fitting parameters shown in Table 1. The surface magnetic field strength is characterized by average $b \sim 4$ (see Fig. 17 in Paper I). We are primarily interested in the polar caps of long period older pulsars which show subpulse drifting. A number of studies have shown that the average emission beam in such cases comprise of a central core surrounded by two concentric rings of conal emission (Rankin 1990, 1993; Mitra & Deshpande 1999; Mitra & Rankin 2002). The presence of two conal rings in such pulsars is also expected from the spark sizes obtained from the PSG model (Mitra et al. 2020). Hence, using $N_{trk} = 2$, the typical spark size can be estimated as $a_{sprk} \sim 23.6$ m, $b_{sprk} \sim 14.9$ m and $h_{\perp} \sim 18.8$ m. The screening factor for the PSG is obtained from eq.(2) as $\eta \sim 0.038$. The drifting periodicity (P_3) in a PSG is given by $P_3 = 1/2\pi\eta \cos \alpha_l$, where α_l is the angle of the local non-dipolar magnetic field with the rotation axis (Mitra et al. 2020). The average $\cos \alpha_l$ is 0.85 for the magnetic field configuration (Fig. 17 in Paper I) and we can estimate P_3 to be $4.9P$.

The two dimensional distribution of the sparks and their evolution with time is shown in Fig.4. The sparks are distributed around two elliptical rings around a central spark in a tightly packed configuration. The details of the sparking distribution for each track is reported in Table 2 and shows the different major (a) and minor (b) axes describing each ring, the maximum number of fully formed spark that can be accommodated along these rings (N_{sprk}), the angular size of the sparks (θ_{sprk}), as explained in section 4. The two bounding points around which the sparking distribution show evolution in opposite directions are $\theta'_s = 264.7^{\circ}$ and $\theta'_e = 84.7^{\circ}$, where the pattern shifts away from

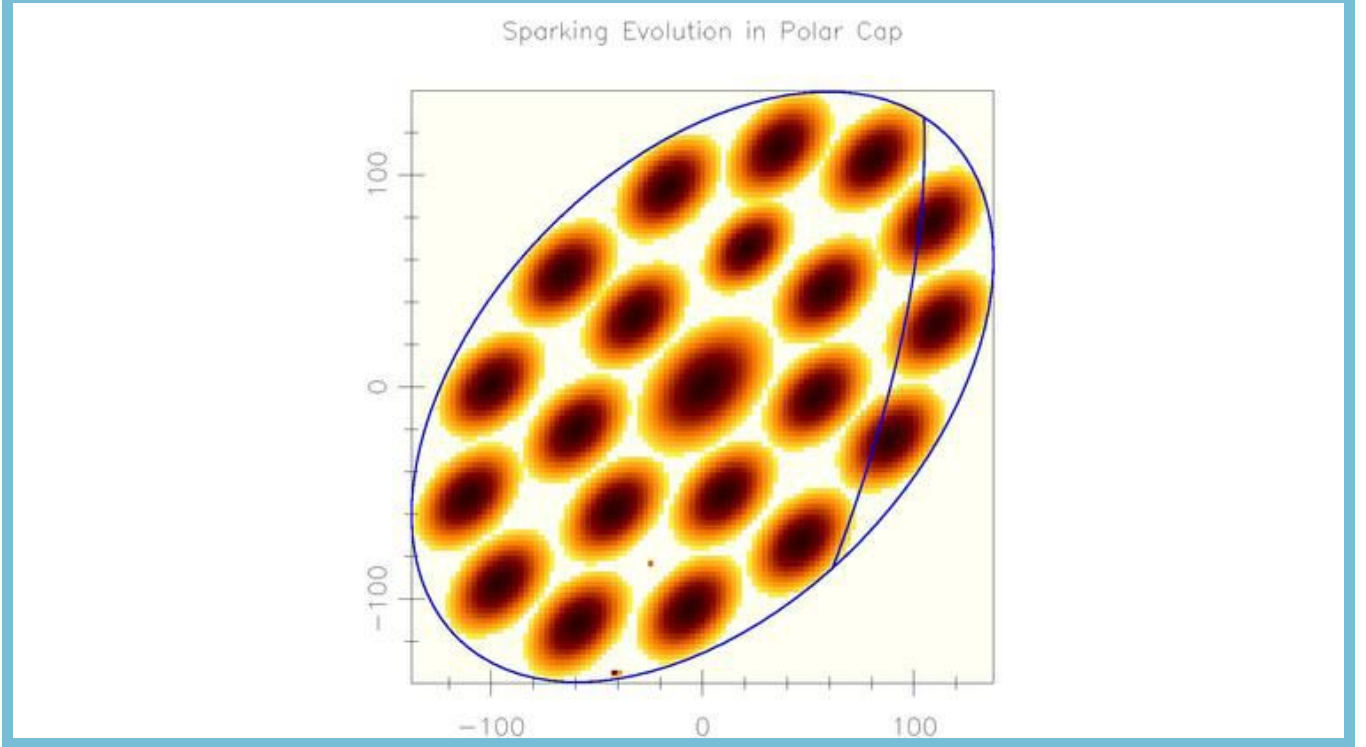


Figure 4. The figure shows the two dimensional distribution of the sparking pattern for an elliptical polar cap with major axis of 127.6 m, minor axis of 80.35 m and tilted by an angle of 45.9° in the plane of the ellipse. The sparks are arranged in two concentric elliptical annulus around a central spark in a tightly packed configuration. The sparking pattern evolves with time to show a clockwise shift in the left half and an anti-clockwise shift in the right half bounded by the points $\theta'_s = 264.7^\circ$ and $\theta'_e = 84.7^\circ$, where the pattern shifts away from θ'_s and converges towards θ'_e . The line of sight (LOS) traverse across the emission beam at an angle $\beta = 3^\circ$ from the center and its imprint on the polar cap is also shown. The dynamical evolution of the sparking distribution across the LOS results in coherent subpulse drifting.

An animation showing the evolution of the sparking configuration with time is available.

Table 2. The details of the sparking distribution in polar cap exhibiting coherent drifting

	i	a_{out}	a_{in}	b_{out}	b_{in}	N_{sprk}	θ_{sprk}	a_{trk}	b_{trk}	$\omega_{u,d}$	
		(m)	(m)	(m)	(m)		(°)	(m)	(m)	(deg s ⁻¹)	
	Outer	1	127.6	80.4	80.4	50.6	13	27.7	104.0	65.5	∓ 5.6
	Inner	2	80.4	33.2	50.6	20.8	7	51.4	56.8	35.7	∓ 10.43

θ'_s and converges towards θ'_e . The rate of shifting of the patterns in the two halves of each ring is estimated as $\omega_{u,d} = \mp \theta_{sprk} / P_3$. The average shift of the sparking pattern during a rotation period ($P = 1$ s) is $h_D = |\omega_{u,d}| \sqrt{a_{trk} b_{trk}} \sim 8.1$ m (see section 4).

We assume the emission to originate from an average height of $30R_S$ where the opening angle of the open field line region is $\rho = 4.55^\circ$. In order to simulate the single pulses exhibiting coherent drifting an outer LOS traverse is considered with $\beta = 3^\circ$, such that $\beta/\rho = 0.66$. We have simulated 128 single pulses using the above setup and the corresponding pulse stack is shown in Fig. 5a. The average profile shows a barely resolved double peaked structure resulting from the shifted non-dipolar polar cap and corresponding shift in the LOS cut across it (see Fig. 4). The single pulses show prominent drift bands with systematic variations across the entire window as expected for coherent

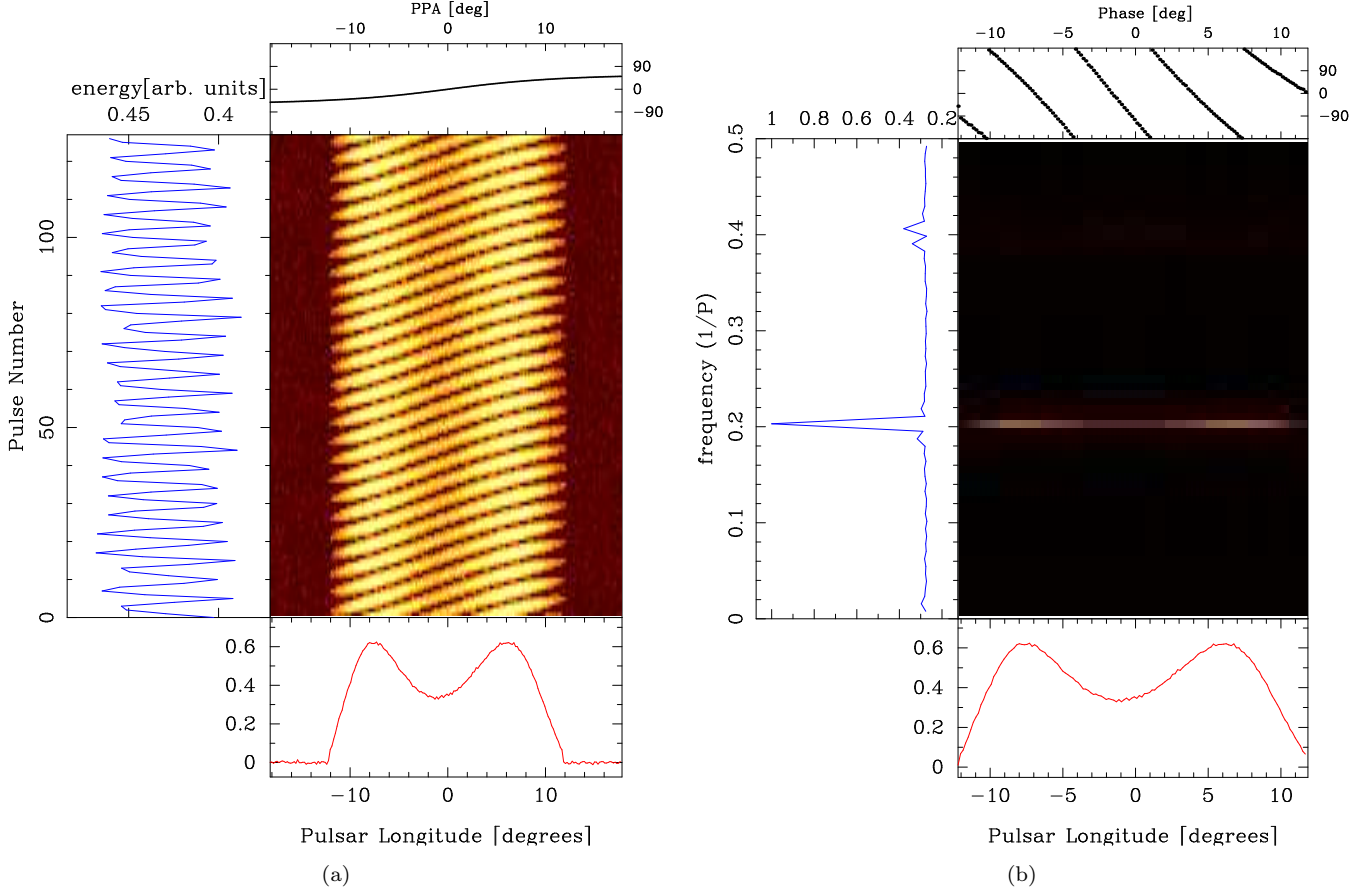


Figure 5. The figure shows single pulse simulations demonstrating the coherent subpulse drifting. (a) Pulse stack with 128 simulated single pulses and (b) Longitude Resolved Fluctuation Spectra (LRFS) across the pulse window. The drifting periodicity, $P_3 = 4.9P$ is seen as a peak frequency, $f_p \sim 0.2$ cycles/ P . The time evolution of the sparking pattern is reflected in the phase behaviour across the profile (top window).

drifting behaviour. The drifting behaviour is characterized using the Longitude Resolved Fluctuation Spectra (LRFS, Backer 1973) as shown in Fig. 5b. The LRFS is estimated by determining the FFT across the 128 pulses along each pulsar longitude within the emission window. The drifting periodicity is seen as the peak amplitude in frequency, $f_p = 0.2$ cycles/ P (left window) while the evolution of the sparking pattern across the LOS is reflected in the large phase variations seen across the emission window (top window). The actual phase variations show continuous change from the leading to the trailing edge of the profile, but has been wrapped around $\pm 180^\circ$ in the figure for convenience of plotting.

5.2. Phase Stationary drifting

The phase-stationary drifting correspond to the cases where the subpulses do not show significant shift in position across the emission window but periodically changes in intensity. As a result the phases associated with the drifting periodicity are relatively flat. The phase-stationary drifting is usually seen in pulsars with multiple components having core-cone profiles where the central core component do not exhibit any periodicity (Rankin 1986; Basu et al. 2019a, 2020a). Such profiles correspond to central LOS traverse of the emission beam with small β . We use the magnetic field configuration of Paper I to study this drifting behaviour where the the star centered dipole is specified as $\mathbf{d} = (d, 45^\circ, 0^\circ)$ and there is one surface dipole $\mathbf{m} = (0.05d, 0^\circ, 0^\circ)$ located at $\mathbf{r} = (0.95R_S, 57.08^\circ, 20.66^\circ)$. The dipolar magnetic axis is tilted by an angle 45° with the rotation axis while the non-dipolar polar cap is located around 20° away from the dipolar polar cap.

The polar cap is highly elliptical in shape and much smaller in size compared to the dipolar case, the fitting parameters shown in Table 1. The surface magnetic field strength is characterized by average $b \sim 19$ (see Fig. 18 in

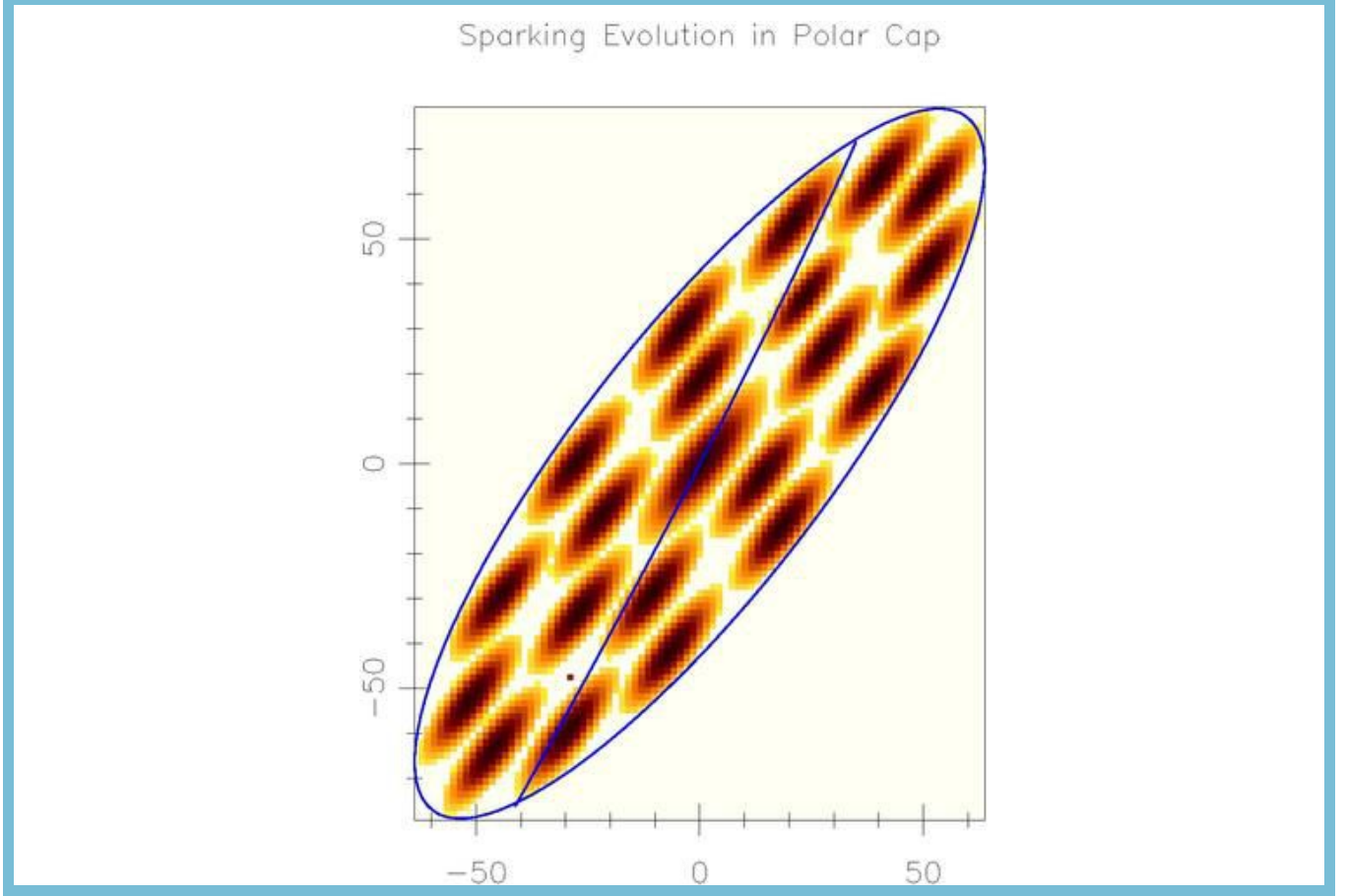


Figure 6. The figure shows the two dimensional distribution of the sparking pattern for an elliptical polar cap with major axis of 75.3 m, minor axis of 21.6 m and tilted by an angle of 52.4° in the plane of the ellipse. The sparks are arranged in two concentric elliptical annulus around a central spark in a tightly packed configuration. The sparking pattern evolves with time to show a clockwise shift in the left half and an anti-clockwise shift in the right half bounded by the points $\theta'_s = 252.1^\circ$ and $\theta'_e = 72.1^\circ$, where the pattern shifts away from θ'_s and converges towards θ'_e . The line of sight (LOS) traverse across the emission beam centrally at an angle $\beta = -0.2^\circ$ and its imprint on the polar cap is also shown. The dynamical evolution of the sparking distribution across the LOS results in phase stationary subpulse drifting in the inner and outer concentric rings, but no periodic behaviour in the central component.

An animation showing the evolution of the sparking configuration with time is available.

Table 3. The details of the sparking distribution in polar cap exhibiting phase stationary drifting

i	a_{out}	a_{in}	b_{out}	b_{in}	N_{sprk}	θ_{sprk}	a_{trk}	b_{trk}	$\omega_{u,d}$	
	(m)	(m)	(m)	(m)		(°)	(m)	(m)	(deg s ⁻¹)	
Outer	1	75.3	47.5	21.6	13.6	13	27.7	61.4	17.6	∓ 2.9
Inner	2	47.5	19.7	13.6	5.6	7	51.4	33.6	9.6	∓ 5.3

Paper I). Assuming $N_{trk} = 2$, the typical spark size can be estimated as $a_{sprk} \sim 13.9$ m, $b_{sprk} \sim 4.0$ m and $h_\perp \sim 7.5$ m. The screening factor for the PSG is obtained from eq.(2) as $\eta \sim 0.021$. The average $\cos \alpha_l$ is 0.8 for the magnetic field configuration (Fig. 18 in Paper I) and we can estimate P_3 to be $9.7P$.

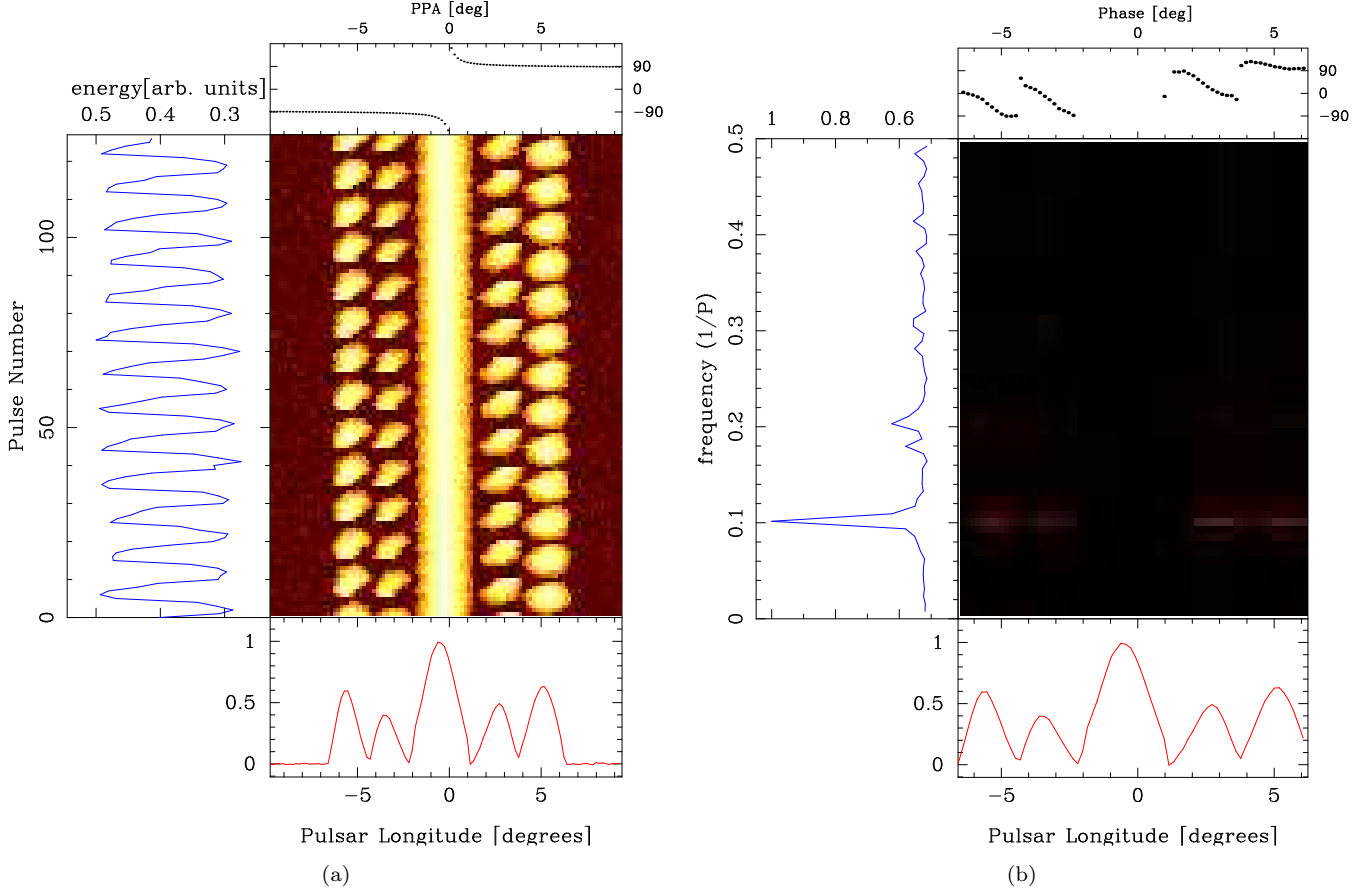


Figure 7. The figure shows single pulse simulations demonstrating the phase stationary drifting. (a) Pulse stack with 128 simulated single pulses. There are five components in the average profile and the central core do not exhibit any periodicity. (b) Longitude Resolved Fluctuation Spectra (LRFS) across the pulse window. The drifting periodicity, $P_3 = 9.7P$ is seen as a peak frequency, $f_p \sim 0.1$ cycles/ P . The time evolution of the sparking pattern is reflected in the phase behaviour across the profile (top window).

The two dimensional distribution of the sparks and their evolution with time is shown in Fig.6. The sparks are distributed around two elliptical rings surrounding a central spark in a tightly packed configuration. The details of the sparking distribution for each track is reported in Table 3 and shows the different major (*a*) and minor (*b*) axes describing each ring, the maximum number of fully formed spark that can be accommodated along these rings (N_{sprk}), the angular size of the sparks (θ_{sprk}), as explained in section 4 and the rate of shifting of the patterns $\omega_{u,d}$. The two bounding points around which the sparking distribution show evolution in opposite directions are $\theta'_s = 252.1^\circ$ and $\theta'_e = 72.1^\circ$, where the pattern shifts away from θ'_s and converges towards θ'_e . The average shift of the sparking pattern during a rotation period ($P = 1$ s) is $h_D \sim 1.7$ m.

We assume the emission to originate from an average height of $30R_S$ where the opening angle of the open field line region is $\rho = 4.55^\circ$. In order to simulate the single pulses exhibiting phase-stationary drifting a central LOS traverse is considered with $\beta = -0.2^\circ$, such that $\beta/\rho = 0.04$. We have simulated 128 single pulses using the above setup and the corresponding pulse stack is shown in Fig. 7a. The average profile has five components where the central core component corresponds to the central region with a constant presence of sparking. As a result the core component does not show any drifting which is an established observational result. The surrounding components show phase stationary drifting with periodic change of intensity but very little systematic variations across the longitudes. The drifting behaviour is characterized using the LRFS as shown in Fig. 7b. The drifting periodicity is seen as the peak amplitude in frequency, $f_p \sim 0.1$ cycles/ P (left window) while small scale phase variations are seen across each component (top window).

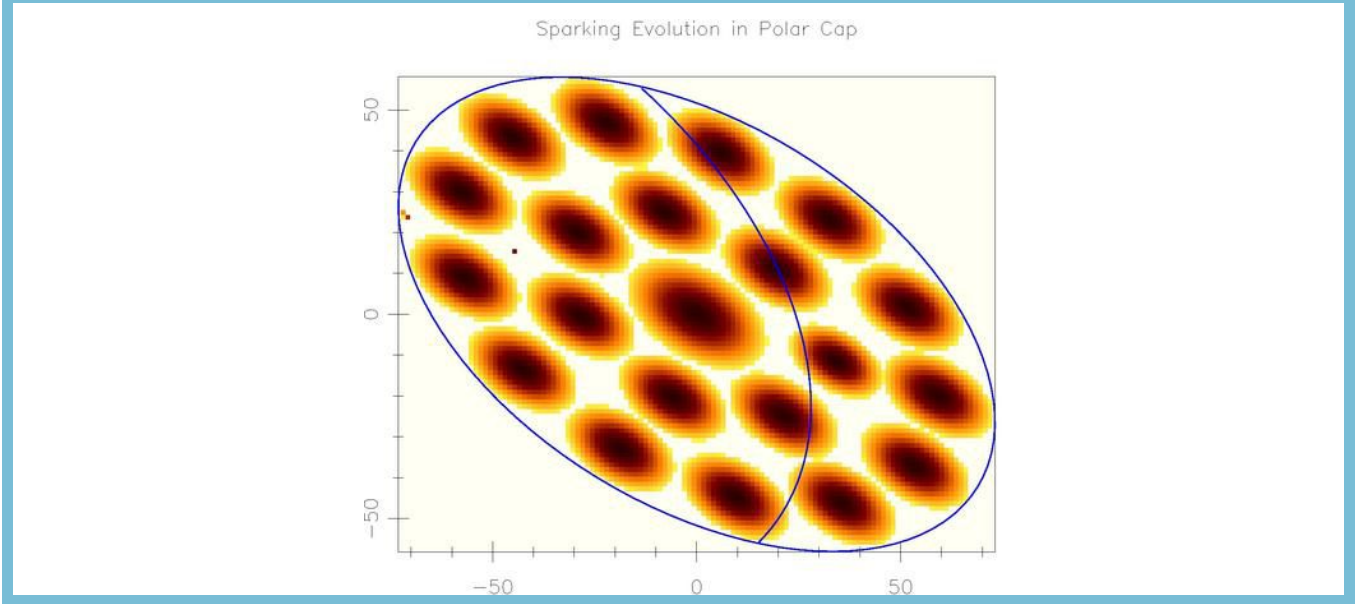


Figure 8. The figure shows the two dimensional distribution of the sparking pattern for an elliptical polar cap with major axis of 62.2 m, minor axis of 36.1 m and tilted by an angle of 148.5° in the plane of the ellipse. The sparks are arranged in two concentric elliptical annulus around a central spark in a tightly packed configuration. The sparking pattern evolves with time to show a clockwise shift in the upper half and an anti-clockwise shift in the lower half bounded by the points $\theta'_s = 169.9^\circ$ and $\theta'_e = -10.1^\circ$, where the pattern shifts away from θ'_s and converges towards θ'_e . The line of sight (LOS) traverses across the emission beam between the center and the edge at an angle $\beta = 2^\circ$ and its imprint on the polar cap is also shown. The dynamical evolution of the sparking distribution across the LOS results in Bi-drifting with opposite drift directions in the upper and lower halves.

An animation showing the evolution of the sparking configuration with time is available.

5.3. Bi-drifting : Reversals in Drift directions

The Bi-drifting phenomenon is a unique drifting behaviour seen in a handful of pulsars (Champion et al. 2005; Weltevrede 2016; Szary & van Leeuwen 2017; Basu & Mitra 2018; Basu et al. 2019b; Szary et al. 2020; Shang et al. 2022) where the drifting direction is opposite in different components of the pulsar profile. These pulsars usually have wider profiles that suggest a small inclination angle θ_d between the rotation and the magnetic axis. The magnetic field configuration used for simulating Bi-drifting in Paper I consisted of a star centered dipole specified as $\mathbf{d} = (d, 5^\circ, 0^\circ)$ and one surface dipole $\mathbf{m} = (0.005d, 0^\circ, 0^\circ)$ located at $\mathbf{r} = (0.95R_S, 5^\circ, 120^\circ)$. The dipolar magnetic axis has a low inclination angle of 5° with the rotation axis, while the non-dipolar polar cap is rotated by a large angle of around 100° away from the dipolar polar cap.

The polar cap is elliptical in shape and is tilted in the opposite direction compared to the previous cases. The parameters of the elliptical fit to the polar cap outline are reported in Table 1. The surface magnetic field strength is characterized by average $b \sim 26$ (see Fig. 19 in Paper I). Assuming $N_{trk} = 2$, the typical spark size can be estimated as $a_{sprk} \sim 11.5$ m, $b_{sprk} \sim 6.7$ m and $h_\perp \sim 8.8$ m. The screening factor for the PSG is obtained from eq.(2) as $\eta \sim 0.013$. The average $\cos \alpha_l$ is 0.79 for the magnetic field configuration (Fig. 19 in Paper I) and the expected P_3 is $15.7P$.

The two dimensional distribution of the sparks and their evolution with time is shown in Fig.8. The sparks are distributed around two elliptical rings surrounding a central spark in a tightly packed configuration. The details of the sparking distribution for each track is reported in Table 4 and shows the different major (a) and minor (b) axes describing each ring, the maximum number of fully formed spark that can be accommodated along these rings (N_{sprk}), the angular size of the sparks (θ_{sprk}), as explained in section 4 and the rate of shifting of the patterns $\omega_{u,d}$. Due to the large shift in the location of the non-dipolar polar cap the sparking distribution evolves along upper and lower parts of the concentric rings, in contrast with the previous cases where the changes happened on the left and right halves. The two bounding points around which the sparking distribution show evolution in opposite directions are $\theta'_s = 169.9^\circ$ and $\theta'_e = -10.1^\circ$, where the pattern shifts away from θ'_s and converges towards θ'_e . The average shift of the sparking pattern during a rotation period ($P = 1$ s) is $h_D \sim 1.2$ m.

Table 4. The details of the sparking distribution in polar cap exhibiting Bi-drifting

	i	a_{out} (m)	a_{in} (m)	b_{out} (m)	b_{in} (m)	N_{sprk}	θ_{sprk} ($^{\circ}$)	a_{trk} (m)	b_{trk} (m)	$\omega_{u,d}$ (deg s^{-1})
Outer	1	62.2	39.2	36.1	22.7	13	27.7	50.7	29.4	∓ 1.8
Inner	2	39.2	16.2	22.7	9.3	7	51.4	27.7	16.0	∓ 3.3

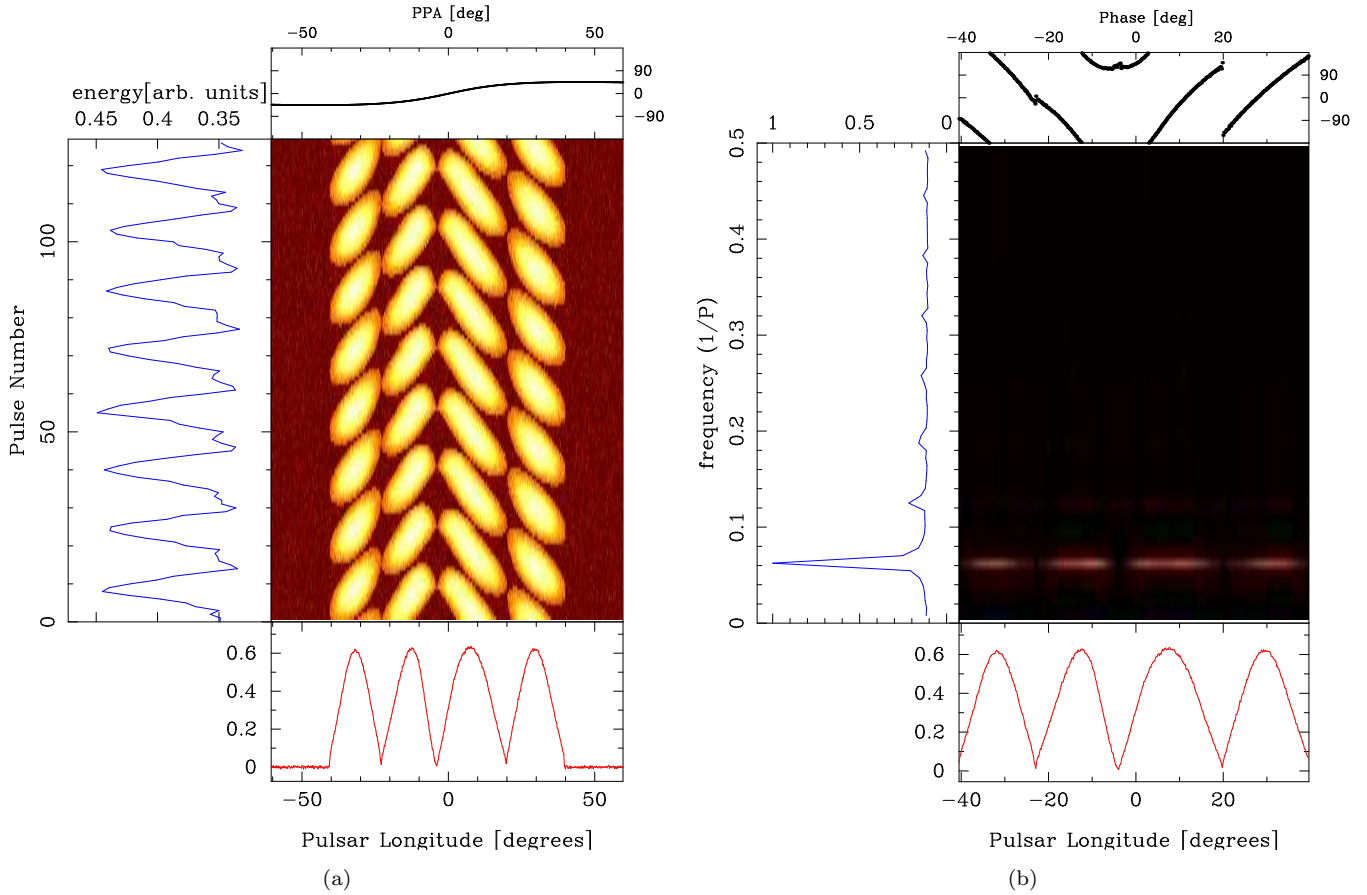


Figure 9. The figure shows single pulse simulations demonstrating Bi-drifting behaviour. (a) Pulse stack with 128 simulated single pulses. There are four components in the average profile with the two leading components drifting in opposite direction to the trailing ones. (b) Longitude Resolved Fluctuation Spectra (LRFS) across the pulse window. The drifting periodicity, $P_3 = 15.7P$ is seen as a peak frequency, $f_p \sim 0.06 \text{ cycles}/P$, in the left window. The time evolution of the sparking pattern is reflected in the phase behaviour across the profile with the first two components showing a negative slope while the phases show a positive slope in their variations in the trailing components (top window).

We assume the emission to originate from an average height of $30R_S$ where the opening angle of the open field line region is $\rho = 4.55^{\circ}$. In order to show the full effect of the Bi-drifting behaviour a LOS traverse halfway between the center and the edge is considered with $\beta = 2^{\circ}$, $\beta/\rho = 0.4$, such that all conal components are visible without being affected by the stationary cone. In contrast to the previous two cases the LOS is roughly perpendicular to the direction of the shifts in the sparking pattern. We have simulated 128 single pulses using the above setup and the corresponding pulse stack is shown in Fig. 9a. The average profile has four components with prominent drifting behaviour where the leading two components have opposite shifts in their drifting pattern compared to the trailing components. The

drifting behaviour is characterized using the LRFS as shown in Fig. 9b. The drifting periodicity is seen as the peak frequency, $f_p \sim 0.06$ cycles/ P (left window), while phase changes show opposite slopes in the leading and trailing components (top window).

6. SUMMARY & CONCLUSION

We have presented a model for the two dimensional distribution of sparking discharges in the IAR above the pulsar polar cap and its evolution with time. The polar cap is dominated by non-dipolar magnetic fields and is smaller in size and usually shifted compared to an equivalent dipolar polar cap. The surface of the polar cap is heated to temperatures $\sim 10^6$ K, around the critical temperature for ionic free flow, resulting in a partially screened gap. The sparking discharges in this system is setup when the temperature goes below the critical level opening up large potential difference for pair cascades to commence. The sparks are essentially a mechanism to regulate the surface temperature where the surface acts as a thermostat. The primary features of the sparking distribution are summarized as follows :

1. The sparks are formed in a tightly packed configuration governed by the surface temperature. The sparks spread out around the point of origin depending on the available potential drop across the field lines, with decreasing particle densities away from the peak location. The region lying between sparks are also heated by diffusion of particles from surrounding sparks and there are no effective gaps between sparks.
2. The sparks have typical durations $\sim 10\text{-}100$ μsec which is the time taken to reach the critical temperature. The sparking is a local event on the surface, governed by the thermostatic regulation, and is unaffected by distant sparks. During the sparking process the charges within the spark lags behind the co-rotation motion due to $\mathbf{E} \times \mathbf{B}$ drift. The surface cooling timescales ~ 100 nsec, is much shorter than the spark duration which ensures that immediately after the cessation of sparking the next spark can be formed at a nearby point.
3. The evolution of the tightly packed sparking distribution in a thermally regulated surface depends on the boundary of the polar cap. No sparking discharges can take place in the closed field line region and hence thermal regulation requires a continuous presence of sparking around the boundary. As the sparks on the boundary drift opposite to the co-rotation direction during their lifetimes, the location of maximally heated points moves around the boundary leading to time evolution of the sparking pattern. The individual sparks are short lived and do not participate in any long term periodic behaviour. The locus of the heating points on the surface around which the subsequent sparking take place show a gradual but continuous shift with time.
4. The evolution of the sparking pattern on the boundary ensures that similar changes take place in the interior as well, since these sparks also affect the heating on the other side. The sparks are setup around concentric rings where two distinct direction of evolution arises bounded by points where the co-rotation direction is normal to the curvature of the boundary. In one half the pattern represents a clockwise shift while in the other half an anti-clockwise shift is setup. As the pattern shifts, gaps open up in the two normal points in each ring where smaller sparks arise to aid the thermal regulation. The evolution of the sparking pattern described above requires the presence of a polar cap boundary with regular curvature like an ellipse or a circle. In case of irregular shapes it is possible that only part of the polar cap shows evolution or the sparking pattern is stationary in case of extremely irregular shapes.
5. Due to differential shift of sparking patterns in two halves the heating location at the center remains stationary with sparks forming at the same place at regular intervals. This resembles the core component in the pulsar profile which do not exhibit any drifting behaviour.

The evolution of the sparking process in IAR was used to simulate the subpulse drifting behaviour in pulsars. We considered three different surface magnetic field configurations, outlined in Paper I, to reproduce the different classes of drifting observed in the pulsar population. In each case detailed characterisation of the sparking properties on the surface was carried out. These provide the template for constraining the physical characteristics of the IAR in pulsars where subpulse drifting has been measured and will be explored in future works. A complete determination of the IAR properties will likely require additional information from X-ray observations to constrain the polar cap temperature and size.

ACKNOWLEDGMENTS

DM acknowledges the support of the Department of Atomic Energy, Government of India, under project no. 12-R&D-TFR-5.02-0700. DM acknowledges funding from the grant “Indo-French Centre for the Promotion of Advanced Research - CEFIPRA” grant IFC/F5904-B/2018. This work was supported by the grant 2020/37/B/ST9/02215 of the National Science Centre, Poland.

REFERENCES

Arumugasamy, P., & Mitra, D. 2019, MNRAS, 489, 4589, doi: [10.1093/mnras/stz2299](https://doi.org/10.1093/mnras/stz2299)

Backer, D. C. 1973, ApJ, 182, 245, doi: [10.1086/152134](https://doi.org/10.1086/152134)

Basu, R., Lewandowski, W., & Kijak, J. 2020a, MNRAS, 499, 906, doi: [10.1093/mnras/staa2398](https://doi.org/10.1093/mnras/staa2398)

Basu, R., & Mitra, D. 2018, MNRAS, 475, 5098, doi: [10.1093/mnras/sty178](https://doi.org/10.1093/mnras/sty178)

Basu, R., Mitra, D., & Melikidze, G. I. 2020b, MNRAS, 496, 465, doi: [10.1093/mnras/staa1574](https://doi.org/10.1093/mnras/staa1574)

Basu, R., Mitra, D., Melikidze, G. I., et al. 2016, ApJ, 833, 29, doi: [10.3847/1538-4357/833/1/29](https://doi.org/10.3847/1538-4357/833/1/29)

Basu, R., Mitra, D., Melikidze, G. I., & Skrzypczak, A. 2019a, MNRAS, 482, 3757, doi: [10.1093/mnras/sty2846](https://doi.org/10.1093/mnras/sty2846)

Basu, R., Paul, A., & Mitra, D. 2019b, MNRAS, 486, 5216, doi: [10.1093/mnras/stz1225](https://doi.org/10.1093/mnras/stz1225)

Champion, D. J., Lorimer, D. R., McLaughlin, M. A., et al. 2005, MNRAS, 363, 929, doi: [10.1111/j.1365-2966.2005.09499.x](https://doi.org/10.1111/j.1365-2966.2005.09499.x)

Cheng, A. F., & Ruderman, M. A. 1980, ApJ, 235, 576, doi: [10.1086/157661](https://doi.org/10.1086/157661)

de Jager, O. C. 2007, ApJ, 658, 1177, doi: [10.1086/511950](https://doi.org/10.1086/511950)

Geppert, U. 2017, Journal of Astrophysics and Astronomy, 38, 46, doi: [10.1007/s12036-017-9460-y](https://doi.org/10.1007/s12036-017-9460-y)

Gil, J., Haberl, F., Melikidze, G., et al. 2008, ApJ, 686, 497, doi: [10.1086/590657](https://doi.org/10.1086/590657)

Gil, J., Lyubarsky, Y., & Melikidze, G. I. 2004, ApJ, 600, 872, doi: [10.1086/379972](https://doi.org/10.1086/379972)

Gil, J., Melikidze, G., & Zhang, B. 2006, ApJ, 650, 1048, doi: [10.1086/506982](https://doi.org/10.1086/506982)

Gil, J., Melikidze, G. I., & Geppert, U. 2003, A&A, 407, 315, doi: [10.1051/0004-6361:20030854](https://doi.org/10.1051/0004-6361:20030854)

Gil, J. A., Kijak, J., & Seiradakis, J. H. 1993, A&A, 272, 268

Gil, J. A., Melikidze, G. I., & Mitra, D. 2002, A&A, 388, 235, doi: [10.1051/0004-6361:20020473](https://doi.org/10.1051/0004-6361:20020473)

Goldreich, P., & Julian, W. H. 1969, ApJ, 157, 869, doi: [10.1086/150119](https://doi.org/10.1086/150119)

Hermsen, W., Hessels, J. W. T., Kuiper, L., et al. 2013, Science, 339, 436, doi: [10.1126/science.1230960](https://doi.org/10.1126/science.1230960)

Hermsen, W., Kuiper, L., Basu, R., et al. 2018, MNRAS, 480, 3655, doi: [10.1093/mnras/sty2075](https://doi.org/10.1093/mnras/sty2075)

Jones, P. B. 1986, MNRAS, 218, 477, doi: [10.1093/mnras/218.3.477](https://doi.org/10.1093/mnras/218.3.477)

Kargaltsev, O., Cerutti, B., Lyubarsky, Y., & Striani, E. 2015, SSRv, 191, 391, doi: [10.1007/s11214-015-0171-x](https://doi.org/10.1007/s11214-015-0171-x)

Kijak, J., & Gil, J. 1998, MNRAS, 299, 855, doi: [10.1046/j.1365-8711.1998.01832.x](https://doi.org/10.1046/j.1365-8711.1998.01832.x)

Krzeszowski, K., Mitra, D., Gupta, Y., et al. 2009, MNRAS, 393, 1617, doi: [10.1111/j.1365-2966.2008.14287.x](https://doi.org/10.1111/j.1365-2966.2008.14287.x)

Lai, D. 2001, Reviews of Modern Physics, 73, 629, doi: [10.1103/RevModPhys.73.629](https://doi.org/10.1103/RevModPhys.73.629)

Lakoba, T., Mitra, D., & Melikidze, G. 2018, MNRAS, 480, 4526, doi: [10.1093/mnras/sty2152](https://doi.org/10.1093/mnras/sty2152)

Melikidze, G. I., Gil, J. A., & Pataraya, A. D. 2000, ApJ, 544, 1081, doi: [10.1086/317220](https://doi.org/10.1086/317220)

Mitra, D. 2017, Journal of Astrophysics and Astronomy, 38, 52, doi: [10.1007/s12036-017-9457-6](https://doi.org/10.1007/s12036-017-9457-6)

Mitra, D., Basu, R., Melikidze, G. I., & Arjunwadkar, M. 2020, MNRAS, 492, 2468, doi: [10.1093/mnras/stz3620](https://doi.org/10.1093/mnras/stz3620)

Mitra, D., & Deshpande, A. A. 1999, A&A, 346, 906, <https://arxiv.org/abs/astro-ph/9904336>

Mitra, D., & Li, X. H. 2004, A&A, 421, 215, doi: [10.1051/0004-6361:20034094](https://doi.org/10.1051/0004-6361:20034094)

Mitra, D., & Rankin, J. M. 2002, ApJ, 577, 322, doi: [10.1086/342136](https://doi.org/10.1086/342136)

Pétri, J., & Mitra, D. 2020, MNRAS, 491, 80, doi: [10.1093/mnras/stz2974](https://doi.org/10.1093/mnras/stz2974)

Press, W. H., Teukolsky, S. A., Vetterling, W. T., & Flannery, B. P. 1992, Numerical recipes in C. The art of scientific computing (Cambridge University press)

Rahaman, S. M., Mitra, D., & Melikidze, G. I. 2020, MNRAS, 497, 3953, doi: [10.1093/mnras/staa2280](https://doi.org/10.1093/mnras/staa2280)

Rankin, J. M. 1986, ApJ, 301, 901, doi: [10.1086/163955](https://doi.org/10.1086/163955)

—. 1990, ApJ, 352, 247, doi: [10.1086/168530](https://doi.org/10.1086/168530)

—. 1993, ApJ, 405, 285, doi: [10.1086/172361](https://doi.org/10.1086/172361)

Ruderman, M. A., & Sutherland, P. G. 1975, ApJ, 196, 51, doi: [10.1086/153393](https://doi.org/10.1086/153393)

Shang, L.-H., Bai, J.-T., Dang, S.-J., & Zhi, Q.-J. 2022, Research in Astronomy and Astrophysics, 22, 025018, doi: [10.1088/1674-4527/ac424d](https://doi.org/10.1088/1674-4527/ac424d)

Sturrock, P. A. 1971, ApJ, 164, 529, doi: [10.1086/150865](https://doi.org/10.1086/150865)

Szary, A. 2013, arXiv e-prints, arXiv:1304.4203, <https://arxiv.org/abs/1304.4203>

Szary, A., Gil, J., Zhang, B., et al. 2017, *ApJ*, 835, 178,
doi: [10.3847/1538-4357/835/2/178](https://doi.org/10.3847/1538-4357/835/2/178)

Szary, A., Melikidze, G. I., & Gil, J. 2015, *MNRAS*, 447,
2295, doi: [10.1093/mnras/stu2622](https://doi.org/10.1093/mnras/stu2622)

Szary, A., & van Leeuwen, J. 2017, *ApJ*, 845, 95,
doi: [10.3847/1538-4357/aa803a](https://doi.org/10.3847/1538-4357/aa803a)

Szary, A., van Leeuwen, J., Weltevrede, P., & Maan, Y.
2020, *ApJ*, 896, 168, doi: [10.3847/1538-4357/ab9226](https://doi.org/10.3847/1538-4357/ab9226)

Sznajder, M., & Geppert, U. 2020, *MNRAS*, 493, 3770,
doi: [10.1093/mnras/staa492](https://doi.org/10.1093/mnras/staa492)

Timokhin, A. N., & Harding, A. K. 2019, *ApJ*, 871, 12,
doi: [10.3847/1538-4357/aaf050](https://doi.org/10.3847/1538-4357/aaf050)

von Hoensbroech, A., & Xilouris, K. M. 1997, *A&AS*, 126,
121

Weltevrede, P. 2016, *A&A*, 590, A109,
doi: [10.1051/0004-6361/201527950](https://doi.org/10.1051/0004-6361/201527950)

Weltevrede, P., Edwards, R. T., & Stappers, B. W. 2006,
A&A, 445, 243, doi: [10.1051/0004-6361:20053088](https://doi.org/10.1051/0004-6361:20053088)

Weltevrede, P., & Johnston, S. 2008, *MNRAS*, 391, 1210,
doi: [10.1111/j.1365-2966.2008.13950.x](https://doi.org/10.1111/j.1365-2966.2008.13950.x)